RSC Advances

PAPER

View Article Online
View Journal | View Issue

Cite this: *RSC Adv.*, 2024, **14**, 34320

Precise air oxidation for continuous production of superparamagnetic Fe_3O_4 nanoparticles at room temperature through a microfilm reactor

Jie Fang, *[a] Hongyun Li,[b] Wangyu Zhu[c] and Baogeng Xie *[d]

Superparamagnetic iron oxide nanoparticles (SPIONs) find vast applications in biomedicine such as drug delivery, magnetic resonance imaging (MRI) contrast agents, cell separation, tissue repair, *etc.* The synthesis of pure and uniform SPIONs involves tedious processes, complex precursors, the assistance of organic solvents, capping agents and/or high temperature. Herein, we report a continuous mass production of pure and uniform SPIONs in aqueous microfilm at room temperature without using any surfactant. The air oxidation rate and nanocrystal formation kinetics were precisely controlled by process intensification in the continuously flowing microfilm. Precise oxidation of Fe(II) is a synergy of disc spinning speed and feeding concentration. The production process was continuous and conducted at room temperature in an aqueous medium with a high yield of 55.4 g h^{-1}. The obtained products were proved to be highly pure through XRD and a colorimetric method. The resulting SPIONs exhibited a narrow size distribution, ranging from 6.5 to 12.6 nm. All sizes of the produced nanoparticles showed characteristic superparamagnetism, with the 12.6 nm SPIONs exhibiting the highest magnetization saturation (M_s) of 87 emu g^{-1}.

Received 24th July 2024
Accepted 16th October 2024

DOI: 10.1039/d4ra05373g

rsc.li/rsc-advances

1 Introduction

Magnetic nanoparticles (MNPs) have become one of the most attractive and widely used inorganic nanomaterials because of their particle size-dependent magnetism, good biocompatibility, high resistivity, and chemical stability.[1–3] Particularly, superparamagnetic Fe_3O_4 nanoparticles, known as SPIONs, are of great interest owing to their unique magnetism. They exhibit zero magnetisation in the absence of an external magnetic field, but can spontaneously be magnetised in response to external magnetic stimuli.[4–6] They have been widely used in chemical sensing,[7] drug delivery,[8] MRI,[9] magnetic hyperthermia therapy,[10] biomolecule separation,[11] magnetic transfections,[12] and so on. Pure superparamagnetism due to Néel relaxation can only be achieved at particle sizes below 12 nm of SPIONs.[13]

The performances of SPIONs strongly depend on their particle size and purity. The presence of bigger particles brings in ferromagnetism and causes magnetization of SPIONs. This can cause undesired aggregation, especially in biomedical applications it affects their blood circulation performance and pharmacokinetics. On the other hand, smaller particles indicate lower saturated magnetization M_s which weakens their response to external magnetization. Impurities are related to the synthesis method, which usually includes under- or over-oxidation/reduction.

Many efforts have been made in synthesising SPIONs with precise size control and high purity in the past decade. Among these, thermal decomposition of chelate precursors in high boiling point organic solvents with the presence of capping and reducing agents has been reported intensively. In 2002, Sun *et al.* first reported synthesizing monodisperse SPIONs with size from 4 nm to 20 nm by the decomposition of Fe(III) acetylacetonate ($Fe(acac)_3$) and partial reduction at 265 °C in the solvent of phenyl ether with the presence of alcohol, oleic acid, and oleylamine.[14] After that, plenty of modified methods were reported using $Fe(acac)_3$ as the precursor to produce high-quality SPIONs.[15–18] Tian *et al.* synthesized ultrafine SPIONs with the size precisely controlled at 1 nm by solvothermal method from the decomposition of $Fe(acac)_3$ with *n*-octylamine as the reducing agent and *n*-octanol as the solvent.[19] Besides, precursors such as iron oleate and iron pentacarbonyl ($Fe(CO)_5$) have also been developed and demonstrated their success in the synthesis of monodisperse SPIONs.[20–23] Besides, SPIONs have also been synthesized *via* reduction of Fe_2O_3 nanoparticles by H_2, oleylamine, or other mild reductants.[24–28]

Indeed, mild reduction of Fe(III) complexes in organic solvents at elevated temperatures always results in highly pure SPIONs. And with the help of capping agents, precise

[a]*School of Food and Pharmacy, Zhejiang Ocean University, 1 Haida'nan Road, Zhoushan 316022, China. E-mail: jiefang10@gmail.com*
[b]*Suzhou Ultranano Technology Co. Ltd, Suzhou 215124, China*
[c]*Zhoushan Hospital, Wenzhou Medical University, Lincheng New District, No. 739 Dingshen Road, Zhoushan 316021, China*
[d]*School of Chemistry and Chemical Engineering, Jinggangshan University, Ji'an 343009, P. R. China. E-mail: liu34111@163.com*

nanoparticle size control is also achievable. Nevertheless, these methods are expensive and difficult to scale up. Stoichiometric co-precipitation of Fe(II) and Fe(III) in alkaline solutions has been widely explored.[29–31] With the help of pH control, the use of surfactants, and/or the assistance of microwave or magnetic fields, the size and morphology of Fe_3O_4 nanoparticles can be improved to some extent.[32–37] However, during the processes, complete deoxygenation of all reactants and careful prevention of air absorption should be carried out to avoid oxidation which will bring in impurities of Fe_2O_3 or FeOOH. Besides, precise size control in aqueous media is much more challenging due to poor control of nucleation and growth rate.

SPIONs can also be produced by proportional oxidation of Fe(II), which is much simpler and more cost-effective, especially being oxidised by air. However, precise 2/3 oxidation of Fe(II) to avoid over-or under-oxidised by-products seems unfeasible in conventional reactors and has been rarely reported.[38,39] Some reported their successes in production of SPIONs from aqueous precipitation of Fe(II) with stirring or aging in conventional vessels to introduce air oxidation. But their proofs of XRD patterns seemed not convincing because the crystal structure and lattice spacing of different form of iron oxides are very close. In fact, according to our experiences, the proportion of Fe(II) and Fe(III) in the final products were always deviated from 1 : 2 when analysed using a more accurately chemical colorimetric method. Moreover, the deviations were always affected by dissolved oxygen content in water, stirring time, stirring speed, vessel volume and *etc.* Thus, to our understanding, the production of SPIONs through proportional oxidation of Fe(II) in conventional vessels were inconsistent and unrepeatable.

The synthesis of SPIONs from stoichiometric co-precipitation of Fe(II) and Fe(III) using a microfilm reactor (MFR) was reported previously.[40] In MFR, the reactant is continuously fed onto the center of a spinning disc followed by spontaneous spreading into a microfilm (Fig. 1a). Both mass and heat transfer are intensified and highly efficient, which enables a rapid and thorough reaction to take place before the reactants leave the disc surface within seconds. However, the synthesis of SPIONs is extremely sensitive to oxygen in the air and dissolved oxygen in the solvent because hematite Fe_2O_3 is thermodynamically more favored. Thus, inert gas purging of the MFR and thorough deoxygenation of all reactants and processes are essential to prevent oxidation. In contrast, if the oxidation can be kinetically precisely controlled, then tedious deoxygenation and inert gas protection processes can be mitigated, and it makes synthesize SPIONs using only Fe(II) be possible. Nevertheless, this has been hardly achieved till now. And it is even more challenging when precise SPIONs size control has to be taken into consideration.

In this article, we report a simple strategy for pure and size tunable SPIONs synthesis from precise oxidation of Fe(II) in a continuously flowing microfilm through air fixation. In the production, $FeCl_2$ aqueous solution and $NH_3 \cdot H_2O$ are used as the only reactants without any surfactant or organic solvent. Furthermore, after understanding of the formation kinetics of SPIONs, we achieve precise control over the key reaction steps, enabling instantaneous room temperature crystallization and narrow particle size distribution. Throughout the entire process, no inert gas purging of the MFR or deoxygenation of the reactants is required, and this makes the production of SPIONs simple, cheap and scalable.

2 Materials and methods

2.1 Materials

Ferrous chloride tetrahydrate ($FeCl_2 \cdot 4H_2O$), ammonia solution (25–28%), 0.2% *o*-phenanthroline, hydroxylamine hydrochloride, ammonium acetate, acetic acid, ammonium fluoride, hydrochloric acid. All reagents were of analytical grade and were used as received without further purification unless otherwise noted. Deionized water was used throughout the experiments.

2.2 Synthesis of SPIONs

The microfilm reactor (MFR) is equipped with a peristaltic pump for reactant injection and a motor controller to set the

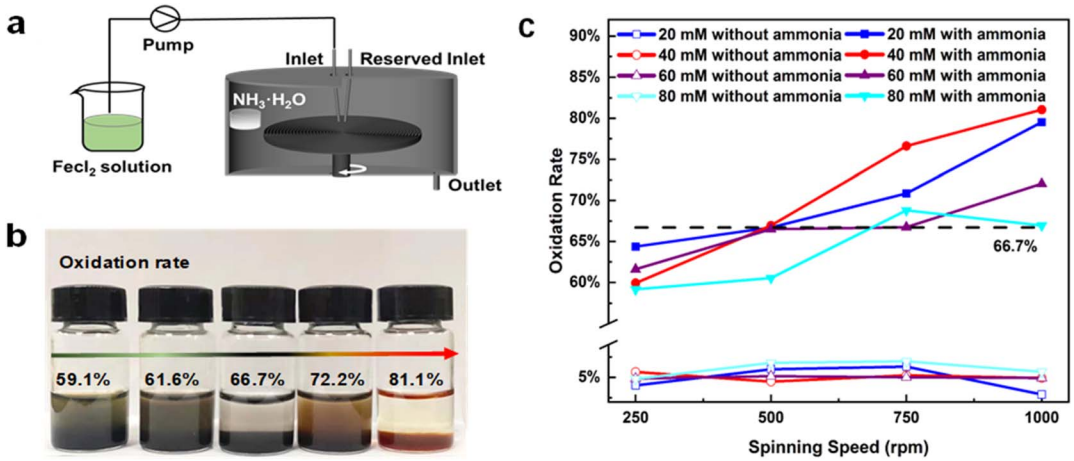

Fig. 1 (a) Schematic illustration of MFR. (b) Photos of products with different oxidation rates obtained at different conditions (from left to right, the samples are 4, 3, 5, 15, and 14). (c) The oxidation rates of products obtained under different spinning speeds, feeding concentrations and with/without ammonia.

spinning speed of the disc. The disc is 22 cm in diameter with the grooved surface at 2 mm intervals (width 0.5 mm, depth 0.2 mm). The injection inlet is 1.5 cm above the center of the disc. The entire reactor interior and the surface of the disc are coated with Teflon.

Before the experiment, a vessel containing ammonia was fixed on the inner wall of the reactor. Then the MFR was set at disc spinning speeds of 250 rpm, 500 rpm, 750 rpm, and 1000 rpm, respectively. Finally, $FeCl_2$ solutions with different concentrations (20 mM, 40 mM, 60 mM and 80 mM) were fed into the MFR. A container was placed under the outlet to collect the products. The products were magnetically separated and washed 3 times with deionised water. Then the wet products were either freeze dried or dried in an oven at 120 °C.

2.3 Surface modification of SPIONs

The SPIONs synthesized by the MFR were first redispersed in deionised water under mechanical stirring, followed by rapid dropwise addition of ammonia to the solution until the pH reached 10 (within 1 minute). This was followed by the addition of ammonium oleate (V(oleic acid)/V(water)/V(ammonia) = 3 : 4 : 2), and stirring was continued for 20 min. Then hydrochloric acid was added dropwise until reaching pH 6–7. Mechanical stirring was continued until complete settling of the product. The product was washed several times with water and ethanol under magnetic separation. Finally, the product was dried under a vacuum.

2.4 Characterizations

XRD analysis was conducted on a Bruker D8 ADVANCE X-ray diffractometer operated at 40 kV and 40 mA using Cu Kα radiation. ICP analysis was conducted with Dual-view Optima 5300 DV ICP-OES system. TEM was performed using FEI Talos F200X. Magnetic properties of SPIONs were analyzed using VSM Lake Shore 7404. DLS was tested by NanoBrook 90Plus. UV-vis Spectrometer was tested by Shanghai Jinghua UV1800PC.

The amount of Fe(II) and Fe(III) is determined by colorimetric method. Fe(II) reacts with *o*-phenanthroline and forms an orange-red complex which shows maximum absorbance at the wavelength (λ_{max}) 510 nm. The color intensity is stable independent of the acidity in the pH ranging from 2 to 9. Five Fe(II) solutions with known concentrations were added to *o*-phenanthroline. The absorption intensity at 510 nm was measured and the standard curve was developed. A collected product was dissolved with concentrated hydrochloric acid followed by added into ammonium acetate buffer solution. Then it was equally divided into two halves. One half was colored with the *o*-phenanthroline solution for 15 min in the dark, and the amount of Fe(II) *m*[Fe(II)] in the product was directly determined against the standard curve. The other half was added into hydroxylamine hydrochloride solution to reduce Fe(III) to Fe(II) followed by colored with the *o*-phenanthroline solution for 15 min in the dark, and the total iron *m*(Fe) measured against the standard curve. Thus, the amount of Fe(III) *m*[Fe(III)] can be calculated by $m[\mathrm{Fe(III)}] = m(\mathrm{Fe}) - m[\mathrm{Fe(II)}]$.[41–43] The oxidation rate was also derived by $m[\mathrm{Fe(III)}]/m(\mathrm{Fe}) \times 100\%$. Table 1 lists the oxidation rates of products obtained under different preparation conditions.

Table 1 The oxidation rates of products obtained under different preparation conditions with ammonia

S/N	Feeding concentration (mM)	Spinning speed (rpm)	Oxidation rate
1	20	250	64.4%
2	40	250	59.9%
3	60	250	61.6%
4	80	250	59.1%
5	20	500	66.7%
6	40	500	66.9%
7	60	500	66.5%
8	80	500	60.5%
9	20	750	70.9%
10	40	750	76.6%
11	60	750	66.7%
12	80	750	68.8%
13	20	1000	79.5%
14	40	1000	81.1%
15	60	1000	72.2%
16	80	1000	66.9%

3 Results

In most of publications, impurity peaks in XRD patterns are identified to determine the compounds and their contents. However, distinguishing different forms of iron oxide from Fe_3O_4 is challenging because their crystal structure and lattice spacing are very close. Mössbauer spectroscopy is a powerful tool in the confirmation of different forms of iron oxide, but the content determination is semi-quantitative. In order to accurately measure the proportions of Fe(II) and Fe(III) in the final product, a colorimetric method was adopted here as described in experimental section.

During the formation of iron oxides, the oxidation occurs on intermediate $Fe(OH)_2$ rather than direct oxidation of Fe(II). This was evidenced that when $FeCl_2$ solution was injected into MFR with the absence of $NH_3 \cdot H_2O$, the oxidation rate was several folds lower at all tested feeding concentrations (20 mM to 80 mM) and spinning speeds (250 rpm to 1000 rpm) than that with the presence of $NH_3 \cdot H_2O$ (a container of concentrated $NH_3 \cdot H_2O$ attached on the inner wall of the reactor) (Fig. 1a). Products with different oxidation rates were collected depending on the parameter settings (Fig. 1b). The oxidation rates was always below 7% without $NH_3 \cdot H_2O$ and above 59% with $NH_3 \cdot H_2O$ in all process conditions, which implies that the oxidation of $Fe(OH)_2$ is more than 8 times higher than that of Fe(II) (Fig. 1c).

The oxidation and precipitation of Fe(II) in an alkaline solution have been studied in different reaction systems.[38,44] In our system, they go through the following reactions:

$$NH_3(g) \rightarrow NH_3 \cdot H_2O(aq) \quad (1)$$

$$Fe^{2+}(aq) + 2OH^-(aq) \rightarrow Fe(OH)_2(s) \quad (2)$$

$$O_2(g) \rightarrow O_2(aq) \quad (3)$$

$$4Fe(OH)_2(s) + O_2(aq) \rightarrow 4FeOOH(s) + 2H_2O(aq) \quad (4)$$

$$Fe(OH)_2(s) + 2FeOOH(s) \rightarrow Fe_3O_4(s) + 2H_2O(aq) \quad (5)$$

$$4Fe(OH)_2(s) + 2H_2O(aq) + O_2(aq) \rightarrow 4Fe(OH)_3(s) \quad (6)$$

$$Fe(OH)_2(s) \rightarrow FeO(s) + H_2O(aq) \quad (7)$$

$$2Fe(OH)_3(s) \rightarrow Fe_2O_3(s) + 3H_2O(aq) \quad (8)$$

The formation rate of $Fe(OH)_2$ in alkali increases with the rise of pH when pH is below 8, but it becomes pH independent when pH is above 8.[45] In our case, NH_3 gas is generated by continuous evaporation from $NH_3 \cdot H_2O$ on the inner wall, and it can be spontaneously absorbed and dissolved into the microfilm because of its high surface to volume ratio (S/V) in the microfilm and high solubility of NH_3. Thus, NH_3 is always sufficiently supplied and does not affect the reaction rate significantly. It was evidenced that pH values in our system did not vary much with values ranging from 11 to 12 where the formation rate of $Fe(OH)_2$ in reaction (2) is independent of pH value. In contrast, dissolved O_2 may not be always sufficiently supplied. It depends on the S/V of the microfilm and consumption rate. At low disc spinning speeds and high Fe(II) concentrations, thin microfilms generate low S/V to decrease the dissolved O_2 concentration, which may lead to insufficient oxidation and cause impurities of $Fe(OH)_2$ or FeO.

At high disc spinning speeds and low Fe(II) concentrations, dissolved O_2 concentration is sufficiently generated. In such cases, apparently, the presence of Fe_2O_3 in the final product is determined by the competing reactions (5) and (6). Formation of $Fe(OH)_3$ in reaction (6) is a zero-order reaction with respect to the concentration of Fe(II). Thus the rate of reaction (6) is independent of the concentration of Fe(II), but dependent of reaction time. Therefore, when reaction (5) is boosted by accelerated mass transfer under high disc spinning speeds, the rate of reaction (6) will not be noticeably raised. In another word, when dissolved O_2 is sufficiently supplied, the purity of

$$\frac{dx}{dt} = k(1-x)^n = k$$

where x is $c(Fe(III))/c(\Sigma Fe)$, t is reaction time, n is reaction order which is 0 in reaction (5), k is reaction rate constant.

FeOOH is thermodynamically unstable, and the rate of reaction (5) is thus determined by the diffusion efficiency of the continuously generated FeOOH. When the micro-mixing is efficient enough, FeOOH can be instantly consumed by reacting with $Fe(OH)_2$, and it in return accelerates the reaction 4 according to Le Chatelier's principle.[46] As a consequence, Fe_3O_4 formation in reaction 5 becomes the dominant product. Fe_3O_4 being the only product is also possible as long as the diffusion of FeOOH is sufficient enough. This provides a window to kinetically control the reaction and produce less thermodynamically favored magnetite SPIONs than hematite Fe_2O_3.

The products' oxidation rate from high feeding concentrations are relatively lower than the low feeding concentrations. This is mainly due to higher feeding concentrations of Fe(II) have higher dissolved oxygen demands. Besides the shortage of dissolved oxygen supply for high feeding concentrations, liquid residence time t_{res} may be another restriction. It should be noted that the oxidation rate even drops when the disc spinning speed is increased from 750 rpm to 1000 rpm at the feeding concentration of 80 mM. This is an indication that the oxidation is suspended and incomplete by the shortened t_{res}. Therefore,

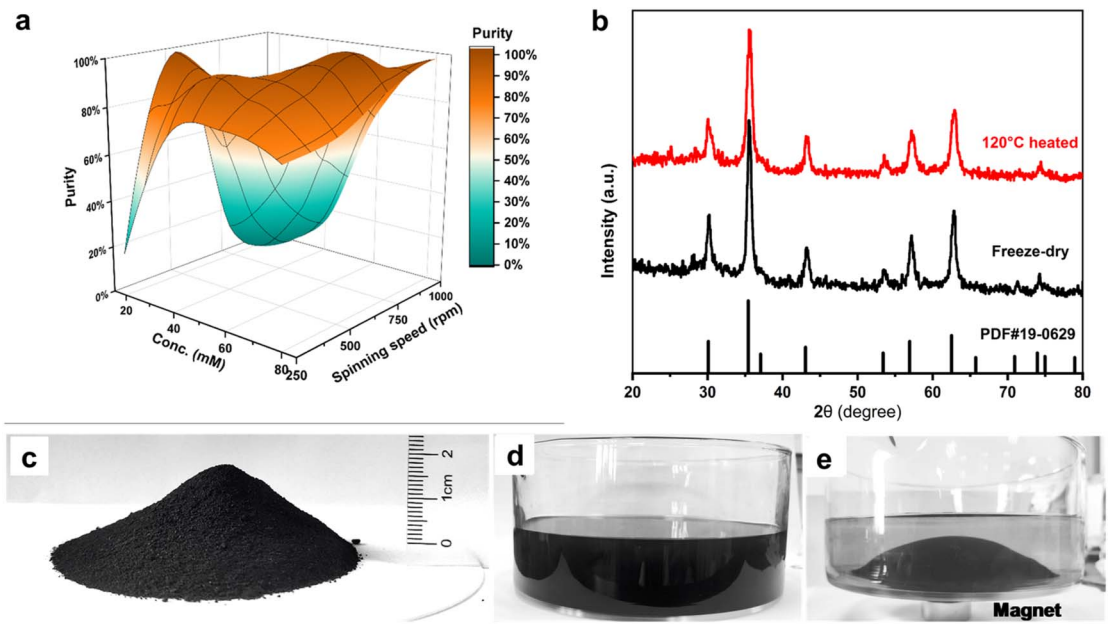

Fig. 2 (a) The purity of the product obtained at different precursor concentrations and different spinning speeds. (b) XRD patterns of SPIONs powder under freeze-dried and 120 °C heated. (c)–(e) Photos of 27.7 g freeze-dried SPIONs powder, as-collected products.

precise oxidation is a combination of spinning speed and feeding concentration at a certain feeding rate.

Pure SPIONs with exact 66.7% oxidation have been achieved under several different conditions, as shown in Fig. 1c and 2a. The products can be simply dried in an oven. But in order to understand the crystal structure and crystallinity, the products were freeze-dried for X-ray diffraction (XRD) analysis. The XRD pattern confirms the pure magnetite structure of SPIONs (JCPDS# 19-0629). The XRD patten of the freeze dried SPIONs is consistent with cubic phase Fe_3O_4. The six diffraction peaks at $2\theta = 30.12°$, $35.69°$, $43.25°$, $53.66°$, $57.34°$, and $62.91°$ correspond to (220), (311), (400), (422), (511), and (440), respectively. No peaks from over/under-oxidised impurities were identified, and the high altitude of the peaks indicates their high crystallinity as shown in Fig. 2b. It has to be noted that the peak altitude is very strong and no improvement has been observed even after being dried at 120 °C, which implies their high degree of crystallinity of the as-prepared products.

The as-prepared products are free of surfactant and any by-product. The supernatant after magnetic separation is colorless and transparent which indicates the completeness of the reaction (Fig. 2c–e). No unreacted Fe was detected when examining the supernatant by inductively coupled plasma (ICP) measurement. The excessive $NH_3 \cdot H_2O$ in the supernatant can be easily collected for re-use. To better characterize the mean diameter and size distribution of SPIONs, they were surface coated with oleic acid to achieve good dispersion in hexane for dynamic light scattering (DLS) and transmission electron microscope (TEM) measurement. SPIONs with mean diameters 6.5 nm, 8.6 nm, 10.6 nm, and 12.6 nm respectively have been

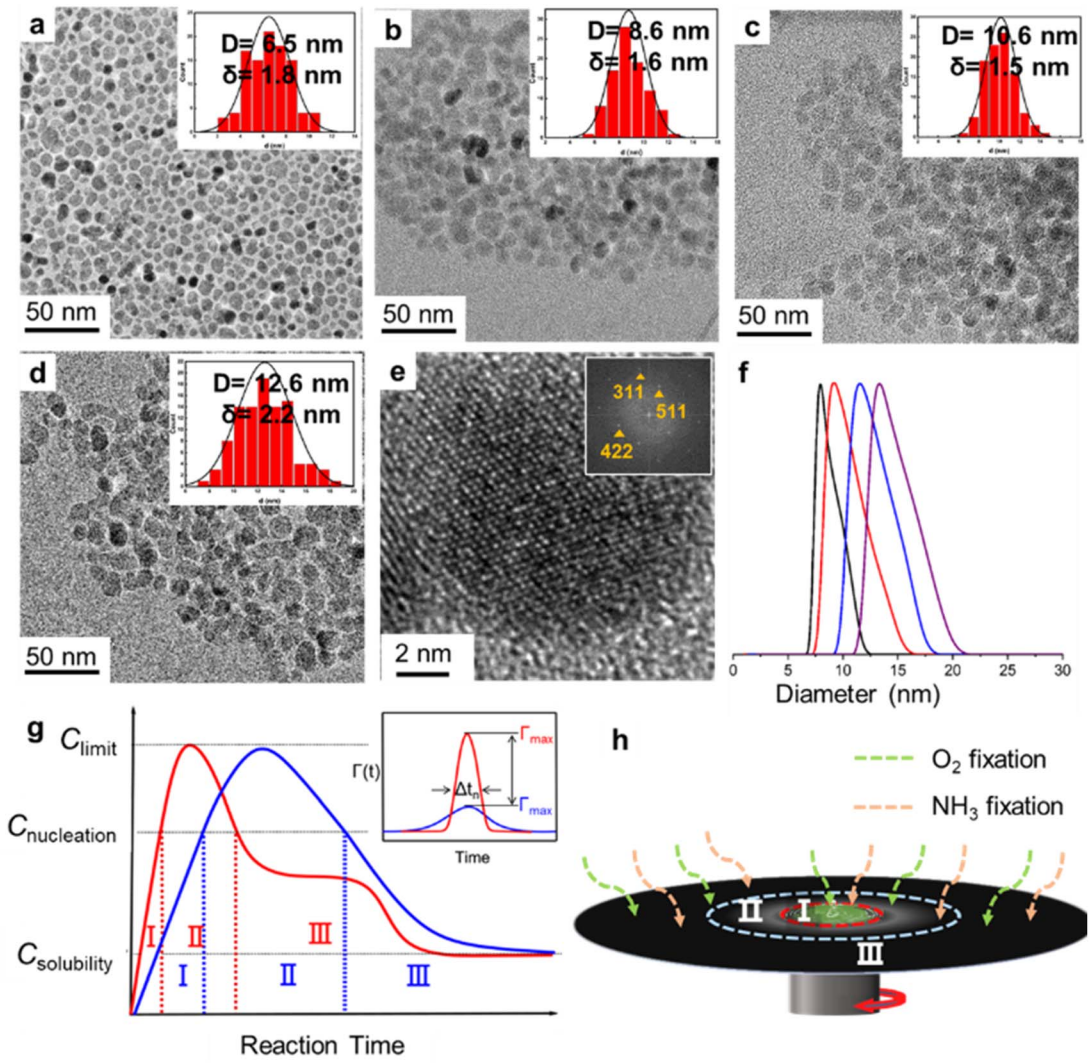

Fig. 3 (a)–(d) TEM images of SPIONs obtained at different conditions and their statistical size distributions. (e) High resolution TEM image of (d) and its FFT pattern. (f) Hydrodynamic sizes of oleic acid coated SPIONs: black, red, blue and brown lines are corresponding to SPIONs in (a–d), respectively. (g) Schematic illustration of LaMer models for SPIONs' formation in the conventional reactor (blue line) and in MFR (red line), zone I to III are monomer generation, nucleation and diffusion growth, respectively. Inset, schematic nucleation functions of SPIONs' formation in the conventional reactor (blue line) and in MFR (red line). (h) Schematic illustration of three zones of LaMer model for the production of SPIONs in MFR.

obtained according to statistical analysis of TEM images (Fig. 3a–d). High resolution TEM image of one SPION nanoparticle displays a clear crystal lattice and its corresponding fast Fourier transform (FFT) confirms the single crystal structure of magnetite (Fig. 3e). The mean diameter measured by DLS is slightly larger than TEM measurement for the respective sample which is due to the surface coating of oleic acid (Fig. 3f).

The particle size and distribution of SPIONs are controlled by nucleation and growth processes. LaMer model describes the kinetics of nanoparticle formation that are controlled by the diffusion of monomers.[47–49] The nucleation and growth processes through the LaMer model can be divided into three steps: a rapid increase in the concentration of free monomers in solution (zone I in Fig. 3g), nucleation of monomers that significantly reduces the concentration of free monomers in solution (zone II in Fig. 3g), and diffusion growth (zone III in Fig. 3g), where the monomers are further consumed by attaching nuclei for size growth. In hydro/solvo-thermal or other conventional processes, monomer gradually ramps-up, and its concentration maintains above the critical nucleation threshold for an extended period. Then nucleation and growth take place by consuming monomers continuously and simultaneously. Limited diffusion rate in conventional reactors could induce high local monomer concentration gradient and cause wide nuclear size distribution which in turn leads to uneven nanoparticle growth. Elevated temperature, high pressure and/or fast stirring are always introduced to accelerate the processes and monomer diffusion so that to narrow the nuclear size distribution. In the diffusion growth zone, the size growth rate should be restricted to allow effective monomers diffusion before growing onto the nuclei. Relatively lower temperatures to slow down the monomer generation and more efficient mixing are favored to minimize the monomer concentration gradient. In many cases, capping agents are applied to slow down the particle growth rate.[50]

In the classical LaMer model, zone II is time dependent behavior of the nucleation rate $I(t)$ which is referred as the nucleation function.[51] The number of nuclei generated in this period determines the number of growing particles, and the time width of zone II, Δt_n, determines the width of the resulting particle-size distribution.[52] (Fig. 3g inset). In MFR, $FeCl_2$ solution is continuously injected onto the center of the spinning disc followed by being spontaneous spread into microfilm where efficient and controlled NH_3 and O_2 fixations take place and causes burst Fe_3O_4 monomer generation (zone I in Fig. 3h) and nucleation (zone II in Fig. 3h). The burst nucleation has an extremely high nucleation rate I_{max} (Fig. 3g inset), and generates large amount of nuclei compared with that of a conventional reactor.

The ultimate mean particle size and size distribution are encoded in the nucleation function $I(t)$. The burst nucleation consumes large quantity of monomers and usually results in restricted particle size with narrow size distribution.[52] However, in our case, the nuclei are efficiently dispersed by the strong shearing forces generated turbulence in which surface tension of the microfilm is broken.[53,54] Meanwhile, the waves and ripples enormously increase S/V, and provide more interfaces for NH_3 and O_2 fixations which in turn give rise to successive monomer generation in zone III. The newly generated monomers are spontaneously consumed for SPIONs size growth without creating new nuclei. Unlike the sharp drop of monomer concentration after nucleation in conventional reactors, the monomer concentration experiences a plateau in the MFR (Fig. 3g). Therefore, the size of SPIONs can be tuned by absorbing the continuously generated and uniformly distributed monomers along the pathway before the spinning disc.

The magnetic properties of obtained SPIONs were measured by a vibrating sample magnetometer (VSM) as shown in Fig. 4. Pure SPIONs with oxidation rate close to 66.67% show significant difference on their magnetization saturations (M_S) while their particle sizes ranges from 6.5 to 12.6 nm as listed in Table 2. And the M_S is size dependent which increases with the growth of SPIONs size. The 12.6 nm SPIONs exhibit the highest M_S of 87 emu g^{-1}. Whereas their magnetic remanence (M_r) and coercivity (H_c) are negligible, which implies these products are superparamagnetic. Although, the under-oxidized product with 59.16% oxidation rate also exhibits low M_r and H_c, it has a very small M_s of 51.70 emu g^{-1}. On the other hand, the over-oxidized

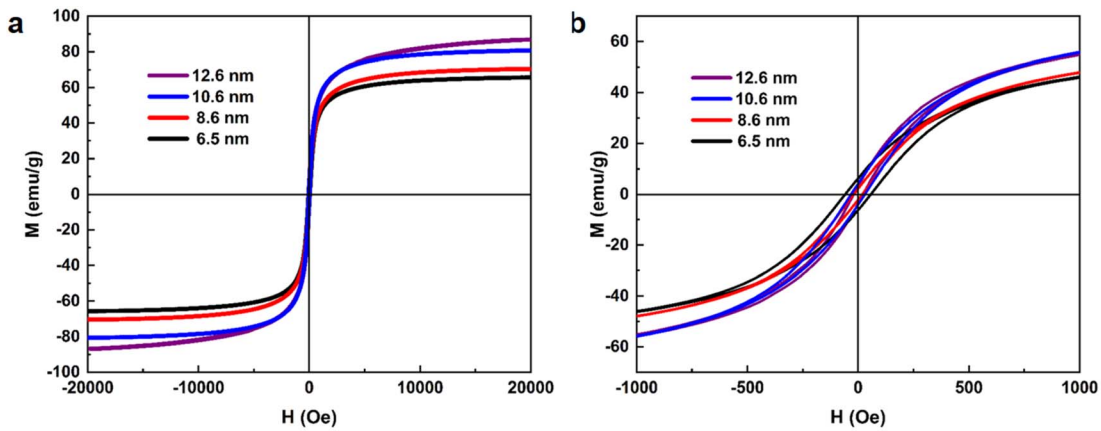

Fig. 4 (a) Magnetic hysteresis loop of SPIONs with different sizes. (b) Magnification of the hysteresis loop near zero fields of (a).

Table 2 A tabular comparison of SPIONs' oxidation rates and magnetic properties obtained by different synthesis parameters

S/N	Synthesis parameter	Oxidation rate	M_s (emu g^{-1})	M_r (emu g^{-1})	H_c (Oe)
5	20 mM to 500 rpm	66.7%	61.17	1.98	19.16
6	40 mM to 500 rpm	66.9%	70.37	2.28	18.90
11	60 mM to 750 rpm	66.7%	80.59	4.23	30.72
16	80 mM to 1000 rpm	66.9%	86.70	3.11	22.47
4	80 mM to 250 rpm	59.1%	51.70	1.47	17.53
14	40 mM to 1000 rpm	81.1%	72.13	6.96	63.14

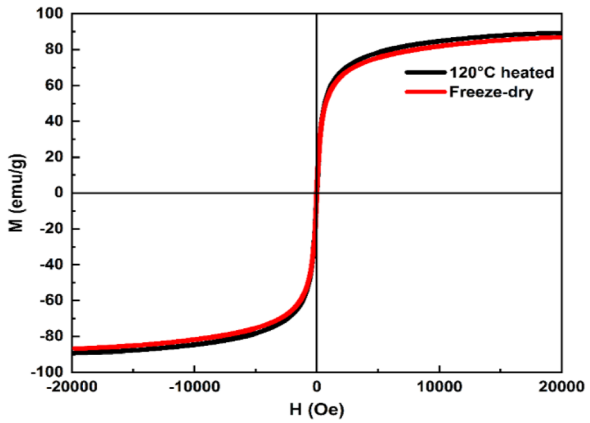

Fig. 5 Magnetic hysteresis loops of SPIONs with freeze-dry and 120 °C heated.

product with 81.06% oxidation rate has a comparable M_s of 72.13 emu g^{-1}, but its M_r and H_c are quite significant and indicate characteristic ferromagnetism. It can be attributed to the co-existence of over-oxidized product of Fe_2O_3 which is a typical ferromagnetic material.

Improved crystallinity by high temperature drying is known to contribute to high M_S.[55] However, this phenomenon has not been observed in our products. The products dried at 120 °C (Fig. 5) do not show any further improvement in M_S. This again indicates that the as-prepared products are highly crystalline which agrees well with HRTEM and XRD measurements.

4 Conclusions

In this article, we have demonstrated a continuous production of semi-monodispersed SPIONs using a MFR. We successfully synthesized highly crystalline single-crystal SPIONs by precisely controlling the reaction kinetics and air oxidation. The preparation process only involves the use of $NH_3 \cdot H_2O$ and $FeCl_2$ as reactants, without the need for expensive iron chelates such as $Fe(acac)_3$ or Fe(III) oleate. Pure SPIONs can be achieved by precise oxidation of Fe(II) at several different combinations of disc spinning speed and feeding concentration. Compared to thermal decomposition methods, we have eliminated the requirement for high boiling point organic solvent, reduction agent and capping agent. The resulting SPIONs exhibit a narrow size distribution, ranging from 6.5 to 12.6 nm. All sizes of the produced nanoparticles showed characteristic superparamagnetism, with the 12.6 nm SPIONs exhibiting the highest M_S of 87 emu g^{-1}, which is close to the theoretical M_s value for bulk magnetite of 92 emu g^{-1}. Consequently, no by-products have been generated, and the product can be simply collected by a magnet without further purification. This not only saves time and cost but also promotes environmental sustainability. Furthermore, the synthesis process is no requirement for inert gas purging in the MFR, nor any need for deoxygenation of the reactants and processes. The production process is continuous, conducted at room temperature in an aqueous medium, with a high yield of 55.4 g h^{-1}. There is no need for downtime, enabling easy scaling-up of production. Thus, the production is extremely low in energy consumption and efficient in yield.

Data availability

The data and materials presented in this study are available on request from the corresponding author.

Author contributions

Conceptualization, J. F. and B. X.; methodology, J. F. W. Z. and H. L.; investigation, J. F. W. Z. and H. L.; data curation, H. L.; writing—original draft, H. L.; writing—review and editing, B. X. and J. F.; supervision, J. F. and B. X.; project administration, J. F.; funding acquisition, J. F. All authors have read and agreed to the published version of the manuscript.

Conflicts of interest

The authors declare no conflicts of interest.

Acknowledgements

This work was financially supported by talent funds of Zhejiang Ocean University, grant number JX6311132223.

References

1 V. Veisi and M. Bagherzadeh, *Desalination*, 2024, **591**, 118001.
2 P. Dong, T. Zhang, H. Xiang, X. Xu, Y. Lv, Y. Wang and C. Lu, *J. Mater. Chem. B*, 2021, **9**, 958–968.

3 Y. Zhao, J. Pan, B. Han, W. Hou, B. Li, J. Wang, G. Wang, Y. He, M. Ma, J. Zhou, C. Yu and S. K. Sun, *ACS Nano*, 2024, **18**, 21112–21124.
4 J. Sikorski, M. Matczuk, M. Stepien, K. Ogorek, L. Ruzik and M. Jarosz, *Nanotechnology*, 2024, **35**, 212001.
5 M. Wang and Z. Zhang, *RSC Adv.*, 2024, **14**, 7891–7902.
6 S. Tong, H. Zhu and G. Bao, *Mater. Today*, 2019, **31**, 86–99.
7 J. Qu, Y. Dong, Y. Wang and H. Xing, *Sens. Biosensing Res.*, 2015, **3**, 74–78.
8 L. Shen, B. Li and Y. Qiao, *Materials*, 2018, **11**, 324.
9 Q. Wu, W. Pan, G. Wu, F. Wu, Y. Guo and X. Zhang, *Atherosclerosis*, 2023, **369**, 17–26.
10 V. Narayanaswamy, S. Sambasivam, A. Saj, S. Alaabed, B. Issa, I. A. Al-Omari and I. M. Obaidat, *Molecules*, 2021, **26**, 796.
11 P. Li, L. Li, Y. Zhao, L. Sun and Y. Zhang, *J. Inorg. Biochem.*, 2016, **156**, 49–54.
12 Y. Wang, H. Cui, K. Li, C. Sun, W. Du, J. Cui, X. Zhao and W. Chen, *PLoS One*, 2014, **9**, 102886.
13 B. Issa, I. M. Obaidat, B. A. Albiss and Y. Haik, *Int. J. Mol. Sci.*, 2013, **14**, 21266–21305.
14 S. Sun and H. Zeng, *J. Am. Chem. Soc.*, 2002, **124**, 8204–8205.
15 S. Belaïd, S. Laurent, M. Vermeersch, L. V. Elst, D. Perez-Morga and R. N. Muller, *Nanotechnology*, 2013, **24**, 055705.
16 N. J. Orsini, B. B. Stojić, V. Spasojević, M. P. Calatayud, N. C vjetićanin and G. F. Goya, *J. Magn. Magn. Mater.*, 2018, **449**, 286–296.
17 J. Muro-Cruces, A. G. Roca, A. López-Ortega, E. Fantechi, D. del-Pozo-Bueno, S. Estradé, F. Peiró, B. Sepúlveda, F. Pineider, C. Sangregorio and J. Nogues, *ACS Nano*, 2019, **13**, 7716–7728.
18 E. Scopel, P. P. Conti, D. G. Stroppa and C. J. Dalmaschio, *SN Appl. Sci.*, 2019, **1**, 147.
19 Y. Tian, B. Yu, X. Li and K. Li, *J. Mater. Chem.*, 2011, **21**, 2476–2481.
20 P. Sharma, N. Holliger, P. H. Pfromm, B. Liu and V. Chikan, *ACS Omega*, 2020, **5**, 19853–19860.
21 K. Woo, J. Hong, S. Choi, H.-W. Lee, J.-P. Ahn, C. S. Kim and S. W. Lee, *Chem. Mater.*, 2004, **16**, 2814–2818.
22 J. Xie, K. Chen, H.-Y. Lee, C. Xu, A. R. Hsu, S. Peng, X. Chen and S. Sun, *J. Am. Chem. Soc.*, 2008, **130**, 7542–7543.
23 J. Park, K. An, Y. Hwang, J.-G. Park, H.-J. Noh, J.-Y. Kim, J.-H. Park, N.-M. Hwang and T. Hyeon, *Nat. Mater.*, 2004, **3**, 891–895.
24 Y. Han, H. Wang, D. Huang, P. Wang, J. Zhang, X. Ren, Y. Meng and B. Lv, *Appl. Surf. Sci.*, 2023, **638**, 158056.
25 H. Wang, B. Liu, G. Yang and C. You, *Int. J. Hydrogen Energy*, 2023, **48**, 16601–16613.
26 A. Bhaskar, M. Assadi and H. N. Somehsaraei, *Energies*, 2020, **13**, 758.
27 Y. Yang, X. Liu, Y. Lv, T. S. Herng, X. Xu, W. Xia, T. Zhang, J. Fang and W. Xiao, Jun Ding, *Adv. Funct. Mater.*, 2015, **25**, 812–820.
28 Z. Kelgenbaeva, B. Murzubraimov, A. A. Tegin, R. Kozlovsky, A. Turdubai kyzy, E. Murzabekova, J. Aidaraliev and B. Dyusheeva, *EPJ Web Conf.*, 2019, **201**, 01002.
29 B. K. Sodipo, O. A. Noqta, A. A. Aziz, M. Katsikini, F. Pinakidou and E. C. Paloura, *J. Alloys Compd.*, 2023, **938**, 168558.
30 E. M. Jafari and I. Hasanzadeh, *Mater. Sci. Eng., B*, 2021, **226**, 115050.
31 A. Ali, H. Zafar, M. Zia, I. U. Haq, A. R. Phull, J. S. Ali and A. Hussain, *Nanotechnol., Sci. Appl.*, 2016, **9**, 49–67.
32 Y. Zhong, L. Yu, Z.-F. Chen, H. He, F. Ye, G. Cheng and Q. Zhang, *ACS Appl. Mater. Interfaces*, 2017, **9**, 29203–29212.
33 L. Wang, S. Su and Y. Wang, *ACS Appl. Nano Mater.*, 2022, **5**, 17565–17575.
34 J. Li, C. Wang, X. Chen, Y. Ma, C. Dai, H. Yang, Q. Li, J. Tao and T. Wu, *RSC Adv.*, 2024, **14**, 7124–7130.
35 F. Hu and Y. S. Zhao, *Nanoscale*, 2012, **4**, 6235–6243.
36 F. Wang, J. Zhang, L. Xu, A. Ma, G. Zhuang, S. Huo, B. Zou, J. Qian, Y. Cui and W. Zhang, *Anal. Chim. Acta*, 2024, **1311**, 342739.
37 J. Wallyn, N. Anton and T. F. Vandamme, *Pharmaceutics*, 2019, **11**, 601.
38 H. Iida, K. Takayanagi, T. Nakanishi and T. Osaka, *J. Colloid Interface Sci.*, 2007, **314**, 274–280.
39 T. Asimakidou, A. Makridis, S. Veintemillas-Verdaguer, M. P. Morales, I. Kellartzis, M. Mitrakas, G. Vourlias, M. Angelakeris and K. Simeonidis, *Chem. Eng. J.*, 2020, **393**, 124593.
40 S. F. Chin, K. S. Iyer, C. L. Raston and M. Saunders, *Adv. Funct. Mater.*, 2008, **18**, 922–927.
41 H. Tamura, K. Goto, T. Yotsuyanagi and M. Nagayama, *Talanta*, 1974, **21**, 314–318.
42 J. Zhu, X. Yang, F. Fan and Y. Li, *Appl. Water Sci.*, 2018, **8**, 228.
43 L. Herrera, P. Ruiz, J. C. Aguillon and A. Fehrmann, *J. Chem. Technol. Biotechnol.*, 1989, **44**, 171–181.
44 Darminto, M. N. Cholishoh, F. A. Perdana, M. A. Baqiya, Mashuri and Y. Cahyono, *AIP Conf. Proc.*, 2011, **1415**, 234–237.
45 B. Morgan and O. Lahav, *Chemosphere*, 2007, **68**, 2080–2084.
46 J. Zhu, L. Li and M. Cao, *Nano Energy*, 2024, **122**, 109300.
47 A. Kirakosyan, J. Kim, S. W. Lee, I. Swathi, S.-G. Yoon and J. Choi, *Cryst. Growth Des.*, 2017, **17**, 794–799.
48 N. T. Thanh, N. Maclean and S. Mahiddine, *Chem. Rev.*, 2014, **114**, 7610–7630.
49 E. C. Vreeland, J. Watt, G. B. S, B. G. Hance, M. J. Austin, A. D. Price, B. D. Fellows, T. C. Monson, N. S. Hudak, L. Maldonado-Camargo, A. C. Bohorquez, C. Rinaldi and D. L. Huber, *Chem. Mater.*, 2015, **27**, 6059–6066.
50 R. Javed, M. Zia, S. Naz, S. O. Aisida, N. ul Ain and Q. Ao, *J. Nanobiotechnol.*, 2020, **18**, 172.
51 S. P. Shields, V. N. Richards and W. E. Buhro, *Chem. Mater.*, 2010, **22**, 3212–3225.
52 F. Wang, V. N. Richards, S. P. Shields and W. E. Buhro, *Chem. Mater.*, 2014, **26**, 5–21.
53 K. S. Iyer, C. L. Raston and M. Saunders, *Lab Chip*, 2007, **7**, 1800–1805.
54 J. R. Burns, C. Ramshaw and R. J. Jachuck, *Chem. Eng. Sci.*, 2003, **58**, 2245–2253.
55 S. Maensiri, M. Sangmanee and A. Wiengmoon, *Nanoscale Res. Lett.*, 2009, **4**, 221–228.